

Probing the Spacetime Structure of Entanglement in Monitored Quantum Circuits with Graph Neural Networks

Javad Vahedi^{1,*} and Stefan Kettemann^{1,†}

¹*Department of Physics and Earth Sciences and Department of Computer Science,
Constructor University, Bremen 28759, Germany*

(Dated: March 24, 2026)

Global entanglement in quantum many-body systems is inherently nonlocal, raising the question of whether it can be inferred from local observations. We investigate this problem in monitored quantum circuits, where projective measurements generate classical records distributed across spacetime. Using graph neural networks (GNNs), we represent individual quantum trajectories as directed spacetime graphs and reconstruct the half-chain entanglement entropy from local measurement data alone. Because information propagates through the network via local message passing, the architecture directly controls the spacetime region over which correlations can be aggregated. By systematically varying this accessible scale—through network depth and hierarchical spacetime coarse-graining—we probe how much measurement information is required to reconstruct global entanglement. We find that prediction accuracy improves as the accessible spacetime region grows and that results from different architectures collapse when expressed in terms of an effective spacetime scale combining depth and coarse-graining. These results demonstrate that the information required to reconstruct global entanglement is organized in spacetime scales and show that graph-based learning architectures provide a controlled operational framework for probing how global quantum correlations emerge from local measurement data.

I. INTRODUCTION

Understanding how global quantum correlations emerge from local information is a central challenge in quantum many-body physics. Entanglement entropy provides a quantitative measure of nonlocal quantum correlations and plays a crucial role in quantum information processing, thermalization, and emergent collective behavior [1, 2]. Because entanglement is inherently nonlocal, determining it typically requires full knowledge of the quantum state, which becomes exponentially costly for large systems. This raises a fundamental question: to what extent can global entanglement properties be inferred from local observations?

Recent developments in monitored quantum systems provide a natural framework in which this question can be explored. In monitored quantum circuits—unitary dynamics interspersed with stochastic projective measurements—the measurement record generates a classical dataset distributed across spacetime. Each measurement outcome provides local information about the system at a particular qubit and time, while the global entanglement structure of the underlying quantum state evolves in response to both unitary dynamics and measurements. Such systems have attracted considerable attention due to the discovery of measurement-induced phase transitions (MIPTs), in which the entanglement scaling changes from a volume law to an area law as the measurement rate increases [3–6]. Although this transition has been extensively studied, the broader question

of whether global entanglement observables can be reconstructed directly from the local measurement record remains largely unexplored.

Machine learning provides a promising framework for addressing this problem. Neural networks have recently been used to represent quantum states, classify phases of matter, and detect phase transitions from experimental or simulated data [7–10]. In the context of monitored circuits, learning-based approaches have been used to identify measurement-induced transitions or decode quantum information from measurement outcomes [11, 12]. However, most architectures employed in these studies—such as fully connected networks—do not explicitly incorporate the spacetime structure of the measurement record. As a result, they provide limited insight into how information propagates across spacetime and how much of the measurement history is required to reconstruct global observables.

In this work, we introduce a framework in which graph neural networks (GNNs) serve as controlled probes of the spacetime structure of entanglement in monitored quantum circuits [13, 14]. Quantum trajectories naturally define directed spacetime graphs whose nodes correspond to qubit–time events and whose edges encode causal and entangling relations. Because GNNs operate through local message passing, information can propagate only along graph edges, such that the network architecture explicitly controls the spacetime region over which correlations are aggregated.

We exploit this property to systematically vary the accessible spacetime scale and investigate how much local measurement information is required to reconstruct global entanglement observables. We compare single-scale architectures, in which the receptive field grows linearly with network depth, with hierarchical architectures

* javahedi@gmail.com

† skettemann@constructor.university

based on iterative 2×2 spacetime blocking that extend the effective spacetime scale through coarse-graining.

We find that the half-chain entanglement entropy of monitored quantum circuits can be accurately reconstructed from local measurement records when information is aggregated over sufficiently large spacetime regions. Prediction accuracy is governed primarily by the accessible spacetime scale: increasing this scale improves performance, and results from different architectures collapse when expressed in terms of a unified effective spacetime scale that combines depth and coarse-graining. These results demonstrate that the information required to reconstruct global entanglement is organized across spacetime scales and establish graph-based learning architectures as an operational framework for probing how global quantum correlations emerge from local measurement data.

II. MODEL AND METHODS

A. Monitored random quantum circuits

We study monitored one-dimensional random quantum circuits with open boundary conditions. Each circuit consists of N qubits and has depth $t_{\max} = 30$, which is sufficient for the entanglement dynamics to approach a steady scaling regime for the system sizes considered. At each time layer, two-qubit Haar-random gates are applied in a brick-wall pattern: even layers act on bonds $(0, 1), (2, 3), \dots$, while odd layers act on $(1, 2), (3, 4), \dots$. After each unitary layer, each qubit is independently projectively measured in the computational basis with probability p . A schematic illustration of the monitored circuit is shown in Fig. 2.

For system sizes $N \in \{8, 10, 12, 14, 16\}$, the circuit dynamics are simulated using exact state-vector evolution. For larger systems, matrix product state simulations are performed using ITensor [15] with adaptive bond dimension to control truncation error. The circuit is initialized in the product state $|0 \cdots 0\rangle$.

For each circuit realization, the supervised learning target is the half-chain von Neumann entropy at the final time t_{\max} ,

$$S_{N/2}(t_{\max}) = -\text{Tr} \rho_L \log \rho_L, \quad (1)$$

where ρ_L denotes the reduced density matrix of the left half of the chain.

To improve generalization across system sizes, we train on the normalized entropy

$$s = \frac{S_{N/2}}{N/2}. \quad (2)$$

This normalization removes the leading extensive scaling with system size and allows the learning task to focus on the underlying intensive structure of the entanglement.

B. Spacetime graph representation

Each circuit realization is mapped to a directed spacetime graph $G = (V, E)$ following the message-passing framework [16–18]. Nodes correspond to spacetime events (i, t) with $i \in \{0, \dots, N-1\}$ and $t \in \{0, \dots, t_{\max}\}$. Directed edges encode causal propagation from past to future. Worldline edges connect $(i, t) \rightarrow (i, t+1)$. For each two-qubit gate acting on bond $(i, i+1)$ at time t , diagonal edges $(i, t) \rightarrow (i+1, t+1)$ and $(i+1, t) \rightarrow (i, t+1)$ are included. No future-to-past edges are introduced. This construction ensures that message passing respects the causal structure of the quantum circuit.

Each node (i, t) carries a feature vector

$$x_{(i,t)} = (m_{i,t}, y_{i,t}, t/t_{\max}, x_L, x_R), \quad (3)$$

where $m_{i,t} \in \{0, 1\}$ is a measurement indicator, $y_{i,t} \in \{-1, +1\}$ is the measurement outcome (set to zero if no measurement occurs). Note that the measurement indicator $m_{i,t}$ ensures that the outcome $y_{i,t} = 0$ is unambiguously interpreted as “no measurement”. and

$$x_L = \frac{i}{N-1}, \quad x_R = 1 - \frac{i}{N-1} \quad (4)$$

encode boundary-aware positional information. Raw qubit indices are not included as features, enabling transferability across system sizes under open boundary conditions. The normalized time coordinate provides the model with global information about circuit depth

C. Single-scale directed graph neural network

We first consider a Single-scale directed GraphSAGE architecture [17]. For node v , the ℓ -th layer update is

$$h_v^{(\ell+1)} = \phi \left(W_0 h_v^{(\ell)} + \frac{1}{|\mathcal{N}^-(v)|} \sum_{u \in \mathcal{N}^-(v)} W_1 h_u^{(\ell)} \right), \quad (5)$$

where $\mathcal{N}^-(v)$ denotes incoming neighbors and ϕ is a ReLU activation. Layer normalization is applied after each layer. The hidden dimension is fixed to 128. The total depth of the Single-scale architecture is denoted by K and varied in $\{1, 2, 3, 4, 6\}$.

Readout is performed using node embeddings at the final time slice $t = t_{\max}$. Let $\mathcal{L} = \{i < N/2\}$ and $\mathcal{R} = \{i \geq N/2\}$ denote the left and right halves. Mean pooling yields

$$z_L = \frac{1}{|\mathcal{L}|} \sum_{i \in \mathcal{L}} h_{(i,t_{\max})}, \quad z_R = \frac{1}{|\mathcal{R}|} \sum_{i \in \mathcal{R}} h_{(i,t_{\max})}. \quad (6)$$

The entropy prediction is obtained via a multilayer perceptron acting on

$$\hat{s} = \text{MLP}([z_L, z_R, |z_L - z_R|, z_L \odot z_R]). \quad (7)$$

This combination captures differences and products between halves, which are natural features for predicting entanglement.

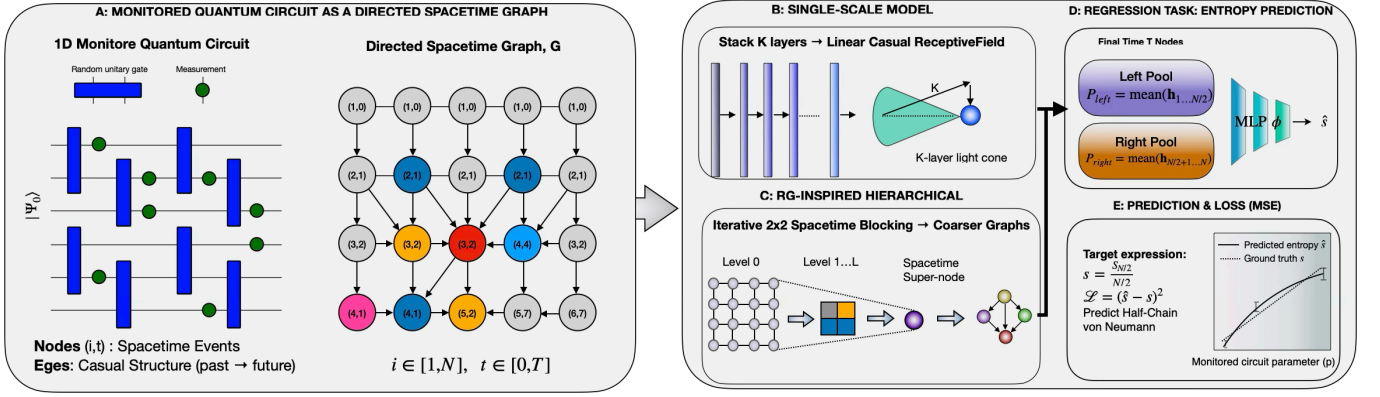


FIG. 1. Overview of the learning framework for predicting entanglement in monitored quantum circuits. (A) A one-dimensional monitored quantum circuit is mapped to a directed spacetime graph G , where nodes correspond to spacetime events (i, t) and edges encode the causal structure of the circuit through worldline and gate-induced connections. Each node carries features derived from the measurement record, including a measurement indicator, measurement outcome, normalized time coordinate, and positional information. (B) Single-scale graph neural network architecture. Stacking K directed GraphSAGE message-passing layers enlarges the causal receptive field linearly with depth, corresponding to a K -layer causal light cone on the spacetime graph. (C) RG-inspired hierarchical architecture. Iterative 2×2 spacetime blocking generates progressively coarser graphs, enabling the network to access larger effective spacetime regions and increasing the receptive field exponentially with the number of coarse-graining levels. (D) Regression task. Node embeddings at the final time slice are pooled separately over the left and right halves of the chain to obtain global representations, which are combined by a multilayer perceptron (MLP) to predict the normalized half-chain von Neumann entropy $s = S_{N/2}/(N/2)$. (E) Prediction and training objective. The model prediction \hat{s} is trained to match the target entropy using the mean squared error loss $\mathcal{L} = (\hat{s} - s)^2$.

D. Single-scale locality and finite-scale interpretation

The depth K of the single-scale network admits a natural interpretation in terms of locality and causal propagation. In strictly unitary local quantum systems, Lieb–Robinson bounds [19, 20] imply

$$\| [O_x(t), O_y(0)] \| \leq C \exp\left(-\frac{|x-y| - v_{\text{LR}} t}{\zeta}\right), \quad (8)$$

which expresses exponential suppression of correlations outside the light cone $|x-y| \leq v_{\text{LR}} t$.

In monitored circuits, the presence of projective measurements breaks unitarity, so rigorous Lieb–Robinson bounds derived for purely unitary dynamics do not directly apply. Nevertheless, the local two-qubit gates impose a finite causal propagation speed determined by the circuit geometry. In the brick-wall circuit used here, information can spread by at most one lattice site per circuit layer. This defines an effective lattice light cone with velocity $v_{\text{lat}} = 1$, in lattice units.

A depth- K directed GNN aggregates information only from nodes connected by directed paths of length at most K . The corresponding truncated backward light cone of a node (i_*, t_*) is therefore contained within

$$\mathcal{R}_K(i_*, t_*) \subseteq \{(i, t) : t_* - K \leq t \leq t_*, |i - i_*| \leq (t_* - t)\}. \quad (9)$$

Thus, the effective spatial scale resolved by the single-scale architecture grows approximately linearly with

depth,

$$\ell_{\text{eff}}^{\text{single}}(K) \sim K. \quad (10)$$

Near the measurement-induced transition, the circuit exhibits a correlation length

$$\xi(p) \sim |p - p_c|^{-\nu}. \quad (11)$$

Since the single-scale network accesses correlations only up to $\ell_{\text{eff}}^{\text{single}}(K)$, we hypothesize that its prediction error may depend on the ratio $\ell_{\text{eff}}^{\text{single}}(K)/\xi(p)$. This motivates a phenomenological finite-scale form

$$\varepsilon(K, p) = K^{-\alpha} f\left(\frac{\ell_{\text{eff}}^{\text{single}}(K)}{\xi(p)}\right), \quad (12)$$

where α and f are determined empirically. This scaling form is treated as a hypothesis and tested against numerical data in Sec. III. In this operational sense, the network depth K acts as an infrared cutoff, limiting the spacetime scale accessible to the model.

E. RG-inspired hierarchical graph neural network

To make the coarse-graining interpretation explicit at the architectural level, we introduce a hierarchical spacetime GNN based on iterative 2×2 blocking.

Starting from the original graph $G^{(0)}$, we define the blocking transformation

$$(i, t) \mapsto (i', t'), \quad i' = \left\lfloor \frac{i}{2} \right\rfloor, \quad t' = \left\lfloor \frac{t}{2} \right\rfloor. \quad (13)$$

Each coarse node aggregates the feature vectors of the four fine nodes in its spacetime block via mean pooling. Directed edges between coarse nodes are induced whenever at least one fine-scale edge connects the corresponding blocks. Duplicate and self-loop edges are removed, producing a new coarse graph $G^{(1)}$. Repeated application generates a hierarchy

$$G^{(0)} \rightarrow G^{(1)} \rightarrow G^{(2)} \rightarrow \dots \quad (14)$$

On each level ℓ , we apply K_ℓ directed GraphSAGE layers before proceeding to the next coarse level. The hierarchical architecture is parameterized by

$$\mathbf{K} = (K_0, K_1, \dots, K_{L-1}), \quad (15)$$

where L is the number of hierarchical levels. The RG depth is defined as $J = L - 1$, equal to the number of coarse-graining steps. In our implementations we consider $\mathbf{K} = (2, 2)$, corresponding to $J = 1$, and $\mathbf{K} = (2, 2, 2)$, corresponding to $J = 2$.

After J blocking steps, the effective spacetime resolution scales approximately as

$$N \rightarrow \frac{N}{2^J}, \quad t_{\max} \rightarrow \frac{t_{\max}}{2^J}. \quad (16)$$

Message passing at the coarsest level probes correlations between blocks of linear size 2^J , yielding an effective scale

$$\ell_{\text{eff}}^{\text{RG}}(J) \sim 2^J K_{\text{top}}, \quad (17)$$

where K_{top} denotes the number of message-passing layers applied at the coarsest level.

Thus, unlike the single-scale architecture where the accessible scale grows linearly with depth, the hierarchical model increases the effective infrared scale exponentially with the RG depth J . While this construction does not constitute an exact renormalization group transformation in the field-theoretic sense, it provides an operational real-space coarse-graining of the spacetime graph. This enables a direct comparison between enlarged receptive field (single-scale model) and explicit blocking (hierarchical model) in probing correlations near the measurement-induced transition.

We emphasize that the blocking transformation operates on the spacetime graph representation and does not correspond to a coarse-graining of the underlying quantum state or density matrix. The hierarchical architecture should therefore be interpreted as an architectural coarse-graining of measurement records rather than a microscopic RG transformation. Its relevance to RG ideas lies in the controlled modification of the effective spacetime scale accessible to the model.

F. Training protocol

Training is performed on mixed system sizes $N \in \{8, 10, 12, 14, 16\}$ using an 80/20 train/validation split at

the circuit-realization level. The loss function is the mean squared error

$$\mathcal{L} = \frac{1}{B} \sum_{i=1}^B (\hat{s}_i - s_i)^2, \quad (18)$$

optimized using the Adam optimizer with learning rate 10^{-3} and weight decay 10^{-5} . Mini-batches contain graphs of varying sizes; batching is handled using PyTorch Geometric's dynamic batching mechanism, which preserves graph boundaries.

During training the model checkpoint with the lowest validation loss is retained. After training, the model is evaluated without fine-tuning on larger systems generated using matrix product state (MPS) simulations.

For comparison between single-scale and hierarchical models, architectures are chosen such that the total number of message-passing layers is comparable (e.g., single-scale $K = 6$ versus hierarchical $(2, 2, 2)$). For hidden dimension 128, the single-scale $K = 6$ model contains approximately 2×10^5 trainable parameters, comparable to the hierarchical $(2, 2, 2)$ model, which has the same number of message-passing layers and therefore nearly identical parameter count. The blocking operations in the hierarchical architecture introduce no additional trainable parameters.

III. RESULTS

In this section we analyze how accurately graph neural networks can reconstruct global entanglement observables from local spacetime measurement records in monitored quantum circuits. Our primary goal is to determine how the prediction accuracy depends on the spacetime scale accessible to the learning architecture.

We proceed in several steps. First, we verify that the neural network accurately reproduces the dependence of half-chain entanglement entropy on the measurement rate. We then investigate how the prediction error depends on the depth of the single-scale GNN, which controls the size of the spacetime region over which information can be aggregated. Finally, we compare this single-scale architecture with the hierarchical model introduced in Sec. II E and examine how prediction accuracy scales with the effective spacetime scale accessible to the network.

A. Entanglement structure and baseline prediction accuracy

Figure 2 shows results obtained using the single-scale architecture with depth $K = 6$. The upper panel shows the normalized half-chain entropy $s = S_{N/2}/(N/2)$ as a function of the measurement rate p for system sizes $N = 14$ and $N = 16$. While $N = 14$ is included in the

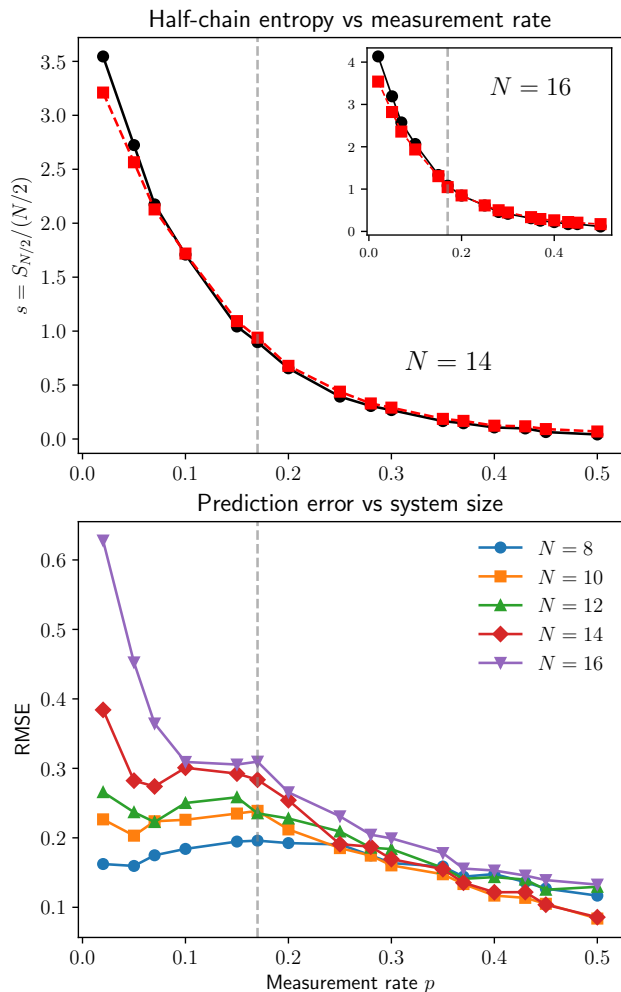


FIG. 2. Baseline behavior of the monitored circuit and prediction accuracy of the graph neural network. Results are obtained using the single-scale GNN with depth $K = 6$. **(Top)** Normalized half-chain entropy $s = S_{N/2}/(N/2)$ as a function of measurement rate p for system sizes $N = 14$ (main panel) and $N = 16$ (inset). Black circles show the exact values obtained from quantum circuit simulations, while red squares denote neural-network predictions. The dashed vertical line indicates the approximate location of the measurement-induced transition at $p_c \approx 0.17$. **(Bottom)** Root-mean-square prediction error (RMSE) as a function of measurement rate for several system sizes. The prediction error is largest in the weak-measurement regime where entanglement is extensive and long-range correlations dominate, and decreases significantly at larger p where frequent measurements suppress entanglement growth.

training set, the system size $N = 16$ is not used during training and therefore provides a direct test of the model’s ability to generalize to larger systems. As expected for monitored random circuits, the entanglement entropy decreases continuously as the measurement rate increases. At small p , the system resides in a volume-law entangled phase characterized by large bipartite entanglement, whereas at large p the entropy approaches

an area-law regime due to frequent measurements that suppress entanglement growth. The dashed vertical line indicates the approximate location of the measurement-induced transition at $p_c \approx 0.17$.

The neural network predictions (red symbols) closely track the exact entanglement values obtained from quantum simulations (black symbols) across the full range of measurement rates. Importantly, this agreement persists even for the unseen system size $N = 16$, demonstrating that the model generalizes beyond the system sizes used during training. This result indicates that the network successfully reconstructs global entanglement observables using only local spacetime measurement data as input, without access to the underlying quantum state. The ability to generalize to larger system sizes suggests that the relevant information for predicting entanglement is encoded in local spacetime patterns of measurements rather than in system-size-specific features.

The lower panel of Fig. 2 shows the root-mean-square prediction error as a function of measurement rate for several system sizes. The error exhibits a clear dependence on both measurement rate and system size. In particular, the prediction error is largest in the weak-measurement regime, where entanglement spreads over large spacetime regions, and decreases substantially as the measurement rate increases. This behavior is consistent with the physical intuition that reconstructing volume-law entanglement requires integrating information over larger spacetime scales than in the strongly measured phase.

We also observe that the prediction error increases with system size for fixed measurement rate, reflecting the growing complexity of the entanglement structure in larger systems. These observations motivate a more detailed investigation of how the accessible spacetime scale of the learning architecture influences prediction accuracy.

B. Depth dependence of the single-scale architecture

We next investigate how the prediction accuracy depends on the depth of the single-scale graph neural network. As discussed in Sec. IIC, the network depth K determines the maximum number of message-passing steps and therefore controls the size of the spacetime neighborhood from which information can be aggregated. Increasing the depth effectively enlarges the causal region accessible to the model, providing an operational probe of the spacetime scale required to reconstruct global entanglement.

The upper panel of Fig. 3 shows the root-mean-square prediction error (RMSE) as a function of network depth for several measurement rates at system size $N = 14$. The prediction error decreases systematically with increasing depth, indicating that deeper networks are able to integrate information over larger spacetime

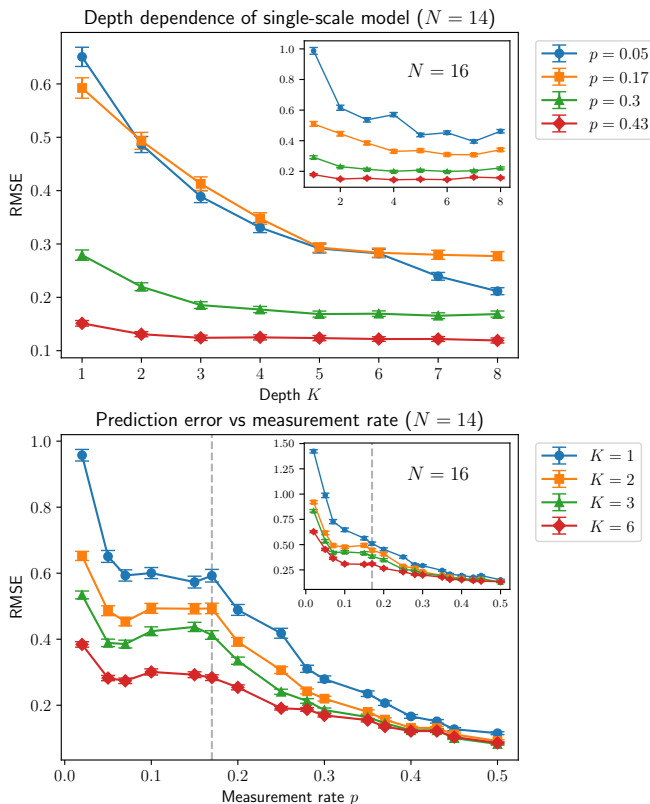


FIG. 3. Depth dependence of the single-scale graph neural network. **(Top)** Root-mean-square prediction error (RMSE) as a function of network depth K for several measurement rates, shown for system size $N = 14$. The inset shows the corresponding results for the unseen system size $N = 16$, demonstrating that the depth dependence generalizes beyond the system sizes used during training. **(Bottom)** Prediction error as a function of measurement rate for several network depths at $N = 14$. The dashed vertical line indicates the approximate measurement-induced transition $p_c \approx 0.17$. The prediction error is largest in the weak-measurement regime and decreases with increasing depth, reflecting the need to integrate information over larger spacetime scales when entanglement is extensive. Insets again show the corresponding behavior for the unseen system size $N = 16$.

regions. This effect is particularly pronounced in the weak-measurement regime ($p = 0.05$), where the system exhibits strong volume-law entanglement. In this regime, shallow networks that access only small spacetime neighborhoods incur large prediction errors, whereas increasing the depth significantly improves the accuracy.

By contrast, in the strongly measured regime ($p = 0.43$) the prediction error is already small for shallow networks and shows only weak dependence on depth. This behavior reflects the reduced spatial extent of entanglement when frequent measurements suppress the growth of quantum correlations. In this regime, the information required to predict the half-chain entropy is largely contained within relatively local spacetime regions.

The inset of the upper panel shows the corresponding

depth dependence for the unseen system size $N = 16$. Despite the model being trained only on system sizes $N \leq 14$, the qualitative behavior remains essentially unchanged. The systematic reduction of prediction error with increasing depth therefore generalizes beyond the system sizes used during training, indicating that the relation between network depth and accessible spacetime scale captures intrinsic properties of the monitored circuit dynamics rather than system-size-specific features.

The lower panel of Fig. 3 further illustrates this behavior by plotting the prediction error as a function of measurement rate for several fixed depths. For shallow networks ($K = 1$ or $K = 2$), the prediction error is large in the weak-measurement regime and decreases gradually as the measurement rate increases. As the depth grows, the error decreases across the entire range of measurement rates, with the largest improvements occurring near and below the measurement-induced transition at $p_c \approx 0.17$. Insets again show the corresponding results for $N = 16$, confirming that the same qualitative trends persist for unseen system sizes.

Taken together, these results support the interpretation that the prediction accuracy of the single-scale architecture is controlled primarily by the spacetime scale accessible to the model. Increasing the network depth enlarges this scale approximately linearly, consistent with the relation $\ell_{\text{eff}}^{\text{single}} \sim K$ introduced in Sec. II C. This observation motivates exploring architectures that can access larger spacetime scales more efficiently, which we address in the following section using a hierarchical coarse-graining approach.

C. Hierarchical architectures and scaling with accessible spacetime scale

We now compare the single-scale architecture with the hierarchical graph neural network introduced in Sec. II E, which combines local message passing with explicit spacetime blocking. The hierarchical model allows the network to access larger effective spacetime regions without requiring a proportionally larger number of message-passing layers.

Figure 4(a) shows the prediction error as a function of measurement rate for the single-scale architecture with depth $K = 6$ together with two hierarchical models, $\text{RG}(2, 2)$ and $\text{RG}(2, 2, 2)$. Across a broad range of measurement rates, the hierarchical architectures achieve prediction accuracy comparable to that of the single-scale model. This is notable because the hierarchical architectures access larger effective spacetime regions through coarse-graining rather than by increasing the number of message-passing steps.

To explore whether prediction accuracy is related to the accessible spacetime scale, we replot the errors as a function of the effective scale ℓ_{eff} defined in Sec. II E. As shown in Fig. 4(b), the prediction error generally decreases as ℓ_{eff} increases. In the present comparison

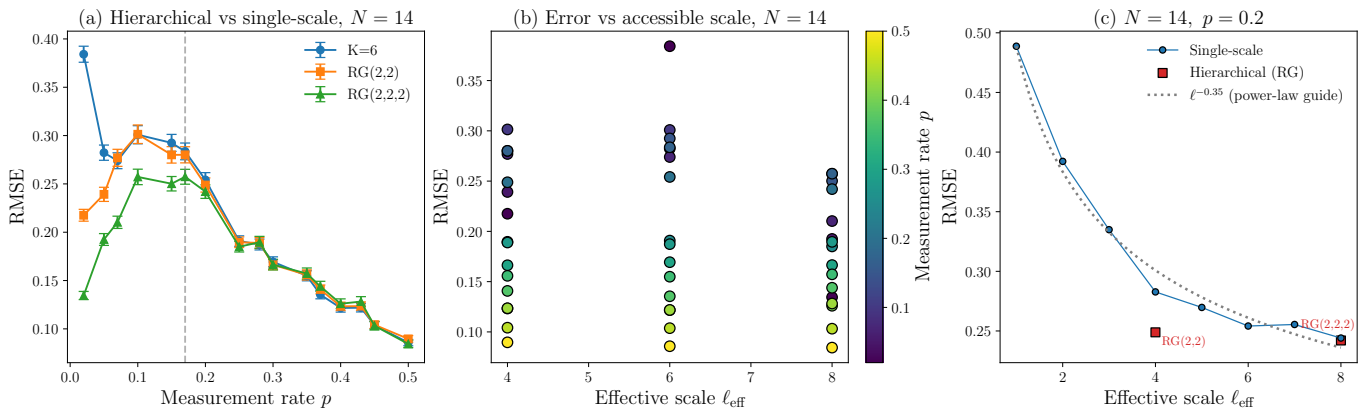


FIG. 4. Comparison between single-scale and hierarchical graph neural network architectures and their dependence on the accessible spacetime scale. (a) Prediction error as a function of measurement rate for the single-scale architecture with depth $K = 6$ and for two hierarchical architectures $RG(2, 2)$ and $RG(2, 2, 2)$ at system size $N = 14$. All models have comparable numbers of message-passing layers but access different effective spacetime scales. The dashed vertical line indicates the approximate measurement-induced transition $p_c \approx 0.17$. (b) Prediction error plotted as a function of the effective spacetime scale ℓ_{eff} defined in Sec. II E. Each point corresponds to a different architecture and measurement rate. Colors indicate the measurement rate p . The error decreases systematically with increasing accessible scale, largely independent of the architectural details. (c) Scaling of the prediction error with accessible scale for a representative measurement rate $p = 0.2$. Blue circles show the single-scale architecture for depths $K = 1 \dots 8$, while red squares show the hierarchical architectures. The dashed curve indicates a power-law guide $\varepsilon \sim \ell_{\text{eff}}^{-0.35}$.

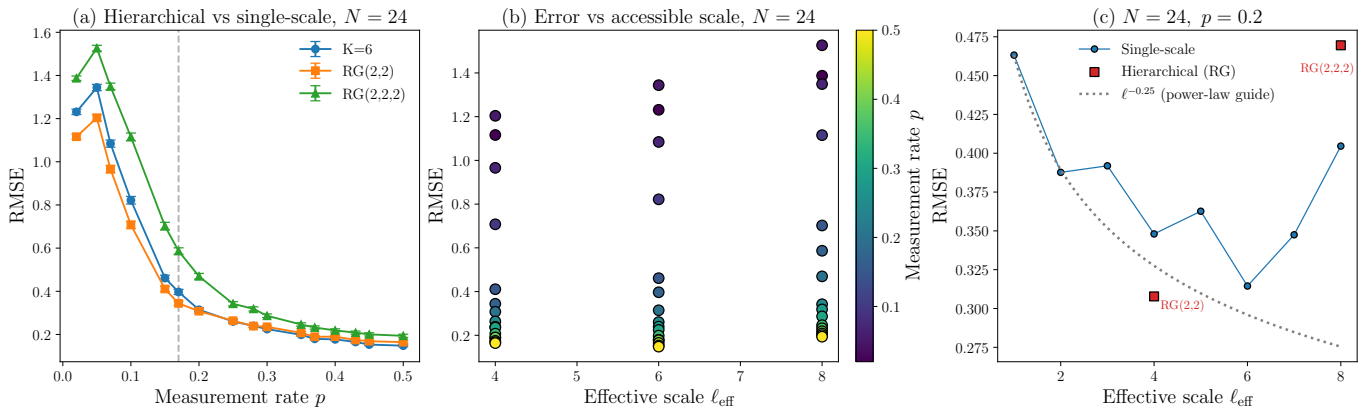


FIG. 5. Same as Fig 4, scaling of prediction error with accessible spacetime scale for an unseen system size $N = 24$. Exact data were generated using tensor-network simulations. The network was trained only on systems with $N \leq 14$.

the architectures correspond to three discrete effective scales, $\ell_{\text{eff}} = 4, 6, 8$, and points at each scale represent results obtained for different measurement rates. Although the scatter reflects the dependence on measurement rate, models with larger accessible spacetime regions tend to achieve lower prediction errors irrespective of the architectural details.

Figure 4(c) further illustrates this trend for a representative measurement rate $p = 0.2$. The prediction error decreases with increasing effective scale and is roughly consistent with a power-law trend $\varepsilon \sim \ell_{\text{eff}}^{-\alpha}$ over the range of scales explored here, with $\alpha \approx 0.35$ for the present dataset. The hierarchical architectures fall close to the same curve obtained for the single-scale models, suggesting that the prediction accuracy is primarily influenced

by the spacetime scale accessible to the network rather than by the specific architectural implementation.

Taken together, these results are consistent with the view that reconstructing global entanglement observables requires integrating measurement information over progressively larger spacetime regions. Architectures that access larger effective scales correspondingly tend to achieve improved predictive performance.

To test whether the observed relationship between prediction accuracy and accessible spacetime scale persists beyond the system sizes used during training, we repeat the analysis for a larger system with $N = 24$. This size was not included in the training data and therefore provides a stringent test of the model's ability to generalize.

Figure 5 presents the same analysis for system size

$N = 24$, where the exact data were generated using tensor-network simulations. Because this system size was not included during training, the prediction errors are generally larger than those observed for $N = 14$. Nevertheless, several qualitative features remain similar.

First, the hierarchical architectures achieve prediction accuracy comparable to that of the single-scale network across a broad range of measurement rates [Fig. 5(a)]. Second, when the prediction error is plotted as a function of the effective spacetime scale [Fig. 5(b)], models with larger accessible scales again tend to exhibit smaller errors despite the increased scatter associated with the larger system size.

Finally, Fig. 5(c) shows the dependence of the error on ℓ_{eff} for a representative measurement rate $p = 0.2$. Although the scaling is less regular than in the $N = 14$ case, the hierarchical architectures remain broadly consistent with the trend observed for the single-scale models. These results suggest that the relationship between prediction accuracy and the accessible spacetime scale persists even for system sizes that lie outside the training distribution.

D. Off-target-time readout of entanglement dynamics

Although the models considered here are trained only to predict the half-chain entropy at the final time t_{max} , the learned spacetime representations can also be probed at earlier times by applying the same readout procedure to intermediate time slices. This provides a useful test of whether the latent representation learned under final-time supervision retains information about the temporal buildup of entanglement.

Figure 6 shows the resulting off-target-time predictions for a representative case in the strongly measured regime, $N = 14$ and $p = 0.4$. Panel (a) compares the exact mean entanglement trajectory $\langle S_{N/2}(t) \rangle$ with predictions obtained from the single-scale model and from the two hierarchical architectures. All three models reproduce the overall growth and late-time saturation of the entanglement entropy, despite having been trained only on the final-time target. The single-scale architecture provides the most accurate reconstruction of the full trajectory, while the hierarchical models capture the coarse trend but smooth over part of the short-time temporal structure.

This difference is reflected in the time-resolved error shown in Fig. 6(b). The single-scale model exhibits the smallest root-mean-square error over most of the evolution, whereas the hierarchical models show larger deviations at early and intermediate times. These deviations are consistent with the explicit temporal coarse-graining built into the hierarchical architectures, which reduces sensitivity to short-time oscillatory features while preserving larger-scale structure.

Panel (c) shows the Pearson correlation between pre-

dicted and exact entropies across individual circuit realizations at each time. The correlation rapidly increases during the evolution and remains substantial over most of the trajectory for all architectures, reaching values of order 0.7–0.8 for the single-scale and RG(2, 2) models at intermediate and late times. Even the deeper hierarchical model RG(2, 2, 2), while less accurate at short times, retains significant predictive correlation once the entanglement growth has developed.

Taken together, these results indicate that final-time supervision induces a latent spacetime representation that contains information about the broader entanglement dynamics, not only the terminal observable used for training. At the same time, the reduced performance of the hierarchical models at short times highlights that off-target-time prediction is sensitive to the temporal resolution of the architecture and should therefore be interpreted as a coarse diagnostic rather than as a fully supervised reconstruction of the entire trajectory.

IV. SUMMARY

In this work we investigated whether global entanglement properties of monitored quantum circuits can be reconstructed directly from local measurement records using graph neural networks. The spacetime structure of the measurement data naturally defines a graph representation, allowing message-passing architectures to aggregate information across both space and time.

We first demonstrated that a graph neural network can accurately predict the half-chain entanglement entropy of monitored random circuits over a broad range of measurement rates. The model reproduces the expected dependence of entanglement on the measurement rate and remains accurate across different system sizes. Importantly, the network generalizes to larger system sizes that were not included during training, indicating that the learned representation captures system-size-independent spacetime features of the measurement dynamics.

We then examined how the architecture controls the spacetime scale accessible to the model. Increasing the depth of a single-scale network reduces the prediction error, consistent with the picture that deeper message passing allows the model to integrate information from larger spacetime regions. Introducing hierarchical coarse-graining further extends the effective spacetime scale that can be accessed with a limited number of layers. The prediction error collapses when plotted against this effective scale, suggesting that the dominant factor governing prediction accuracy is the spacetime region from which the model can collect information.

Finally, we showed that the learned representations retain information about the temporal buildup of entanglement. Although the networks were trained only on the final-time entropy, the same readout procedure applied to intermediate time slices recovers the overall growth of the entanglement entropy and maintains significant correla-

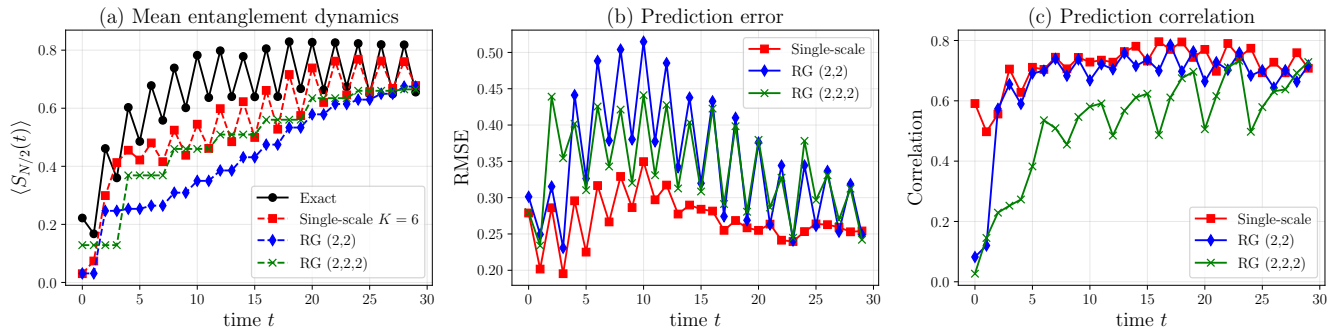


FIG. 6. Off-target-time readout of entanglement dynamics for system size $N = 14$ and measurement rate $p = 0.4$. The models are trained only on the final-time entropy at $t_{\max} = 30$, but are evaluated here by applying the learned readout to intermediate time slices. (a) Mean half-chain entropy $\langle S_{N/2}(t) \rangle$ as a function of time for the exact dynamics, the single-scale model with depth $K = 6$, and the two hierarchical architectures RG(2,2) and RG(2,2,2). All models capture the overall entanglement growth and saturation, with the single-scale model showing the closest agreement to the exact trajectory. (b) Time-resolved root-mean-square prediction error. The hierarchical models exhibit larger deviations at short and intermediate times, consistent with their reduced temporal resolution due to coarse-graining. (c) Pearson correlation between predicted and exact entropies across circuit realizations at each time. Despite being trained only on the final-time target, all models retain substantial trajectory-level correlation over much of the evolution.

tion with the exact dynamics. Influence maps further reveal that the networks rely on localized spacetime regions whose extent grows with architectural depth, providing a qualitative visualization of the effective spacetime scale explored by the model.

These results highlight the potential of graph-based learning approaches for extracting physically meaningful observables from local measurement data in quantum many-body systems. More broadly, they suggest that machine-learning architectures can serve as controlled probes of the spacetime structure underlying complex quantum dynamics.

Several directions for future work remain open. It would be interesting to apply similar approaches to other observables, including operator spreading and correlation functions, and to investigate whether such models can identify critical behavior near measurement-induced phase transitions. Recent work has also highlighted the rich structure of measurement-induced information, including finite-time teleportation transitions in monitored circuits [21] and universal long-distance features of measurement-induced entanglement in many-body quantum states [22]. Extending the present reconstruction framework to probe such phenomena directly from measurement records could provide new insights into the spacetime organization of measurement-induced correlations. Another promising direction is to explore adaptive or physics-informed hierarchical architectures that more closely mirror the underlying causal structure of monitored quantum circuits [23].

V. ACKNOWLEDGMENTS

J.V. acknowledges the Ataro Group for generously providing office space and computational resources that facilitated the completion of this work.

Appendix A: Measurement probability under spacetime blocking

In the hierarchical architecture introduced in Sec. II E, the spacetime graph representation of a monitored circuit is coarse-grained through iterative 2×2 blocking. This construction operates on the graph representation used by the neural network and does not define a renormalization-group transformation of the underlying circuit dynamics. In particular, the measurement probability p of the monitored circuit is not rescaled under this architectural coarse-graining.

It is nevertheless instructive to contrast this construction with a hypothetical renormalization of the circuit itself. If two consecutive time layers of the circuit were coarse-grained into a single effective layer, each qubit would experience two independent opportunities for a projective measurement. In that case the probability of observing at least one measurement event would be

$$p' = 1 - (1 - p)^2, \quad (\text{A1})$$

which corresponds to the probability that at least one of the two measurement attempts occurs. For small p , this yields $p' \approx 2p$. Such a transformation would therefore modify the effective measurement rate of the circuit.

The hierarchical graph construction used in this work differs fundamentally from this scenario. The coarse-graining step groups multiple spacetime nodes of the

measurement record into a single coarse node, but it does not generate a new circuit ensemble or modify the physical measurement process. Instead, the feature vector associated with a coarse node aggregates the features of the corresponding fine nodes (via mean pooling in our implementation). Consequently, the network receives an averaged summary of the measurement information within each spacetime block rather than a renormalized measurement probability.

In this sense the blocking procedure should be interpreted as an architectural coarse-graining of the spacetime graph representation rather than a renormalization of the monitored circuit itself. The physical parameter p therefore remains unchanged throughout the hierarchical construction, while the effective spacetime scale accessible to the model increases with the RG depth.

Appendix B: Spacetime influence maps

To gain qualitative insight into what spacetime regions of the measurement record contribute to the neural-network prediction, we compute influence maps that quantify the sensitivity of the predicted entropy to local measurement events.

For a given spacetime location (i, t) , the influence is estimated by measuring how strongly perturbations of the corresponding input feature modify the predicted half-chain entropy $S_{N/2}$. This produces a spacetime map that highlights the regions of the measurement record that most strongly affect the model output.

Figure 7 compares the resulting influence patterns for

representative architectures. The upper row shows the influence maps for three different models at final time: a shallow single-scale network with depth $K = 2$, a deeper single-scale network with $K = 6$, and a hierarchical architecture RG(2, 2, 2). In each panel, the red cross marks the spacetime location associated with the final-time readout near the entanglement cut.

Several qualitative features are apparent. The shallow network exhibits a highly localized influence region, indicating that the prediction depends primarily on measurements in a small neighborhood of the readout location. Increasing the depth of the single-scale network significantly enlarges the region of influence, reflecting the increased spacetime scale accessible through message passing. The hierarchical architecture produces an extended but coarser influence region, consistent with its multiscale coarse-graining structure.

The lower row illustrates the dependence of the influence region on the readout time t_r . As the readout time increases, the dominant influence shifts upward in time and broadens in spacetime, indicating that later predictions depend on a larger portion of the preceding measurement history. The resulting patterns resemble a causal spacetime region surrounding the readout slice, qualitatively consistent with the propagation of information in monitored quantum circuits.

These influence maps provide an intuitive visualization of how the graph neural network integrates information from the measurement record and support the interpretation developed in the main text: the architectural depth and hierarchy control the effective spacetime scale over which the model aggregates information.

-
- [1] J. Emerson, Y. S. Weinstein, M. Saraceno, S. Lloyd, and D. G. Cory, Pseudo-random unitary operators for quantum information processing, *Science* **302**, 2098–2100 (2003).
 - [2] R. Oliveira, O. C. O. Dahlsten, and M. B. Plenio, Generic entanglement can be generated efficiently, *Phys. Rev. Lett.* **98**, 130502 (2007).
 - [3] Y. Li, X. Chen, and M. P. A. Fisher, Quantum zeno effect and the many-body entanglement transition, *Phys. Rev. B* **98**, 205136 (2018).
 - [4] B. Skinner, J. Ruhman, and A. Nahum, Measurement-induced phase transitions in the dynamics of entanglement, *Phys. Rev. X* **9**, 031009 (2019).
 - [5] A. Chan, R. M. Nandkishore, M. Pretko, and G. Smith, Unitary-projective entanglement dynamics, *Phys. Rev. B* **99**, 224307 (2019).
 - [6] M. J. Gullans and D. A. Huse, Dynamical purification phase transition induced by quantum measurements, *Phys. Rev. X* **10**, 041020 (2020).
 - [7] T. Ohtsuki and T. Ohtsuki, Deep learning the quantum phase transitions in random two-dimensional electron systems, *Journal of the Physical Society of Japan* **85**, 123706 (2016).
 - [8] G. Carleo and M. Troyer, Solving the quantum many-body problem with artificial neural networks, *Science* **355**, 602–606 (2017).
 - [9] J. Carrasquilla and R. G. Melko, Machine learning phases of matter, *Nature Physics* **13**, 431–434 (2017).
 - [10] P. Mehta, M. Bukov, C.-H. Wang, A. G. Day, C. Richardson, C. K. Fisher, and D. J. Schwab, A high-bias, low-variance introduction to machine learning for physicists, *Physics Reports* **810**, 1–124 (2019).
 - [11] H. Dehghani, A. Lavasani, M. Hafezi, and M. J. Gullans, Neural-network decoders for measurement induced phase transitions, *Nature Communications* **14**, 10.1038/s41467-023-37902-1 (2023).
 - [12] F. El Ayachi, H. Ait Mansour, and M. El Baz, Quantum neural networks to detect entanglement transitions in quantum many-body systems, *Physica Scripta* **100**, 016001 (2024).
 - [13] F. Scarselli, M. Gori, A. C. Tsoi, M. Hagenbuchner, and G. Monfardini, The graph neural network model, *IEEE Transactions on Neural Networks* **20**, 61–80 (2009).
 - [14] W. L. Hamilton, R. Ying, and J. Leskovec, *Inductive representation learning on large graphs* (2017).
 - [15] M. Fishman, S. R. White, and E. M. Stoudenmire, The ITensor Software Library for Tensor Network Calculations, *SciPost Phys. Codebases*, 4 (2022).

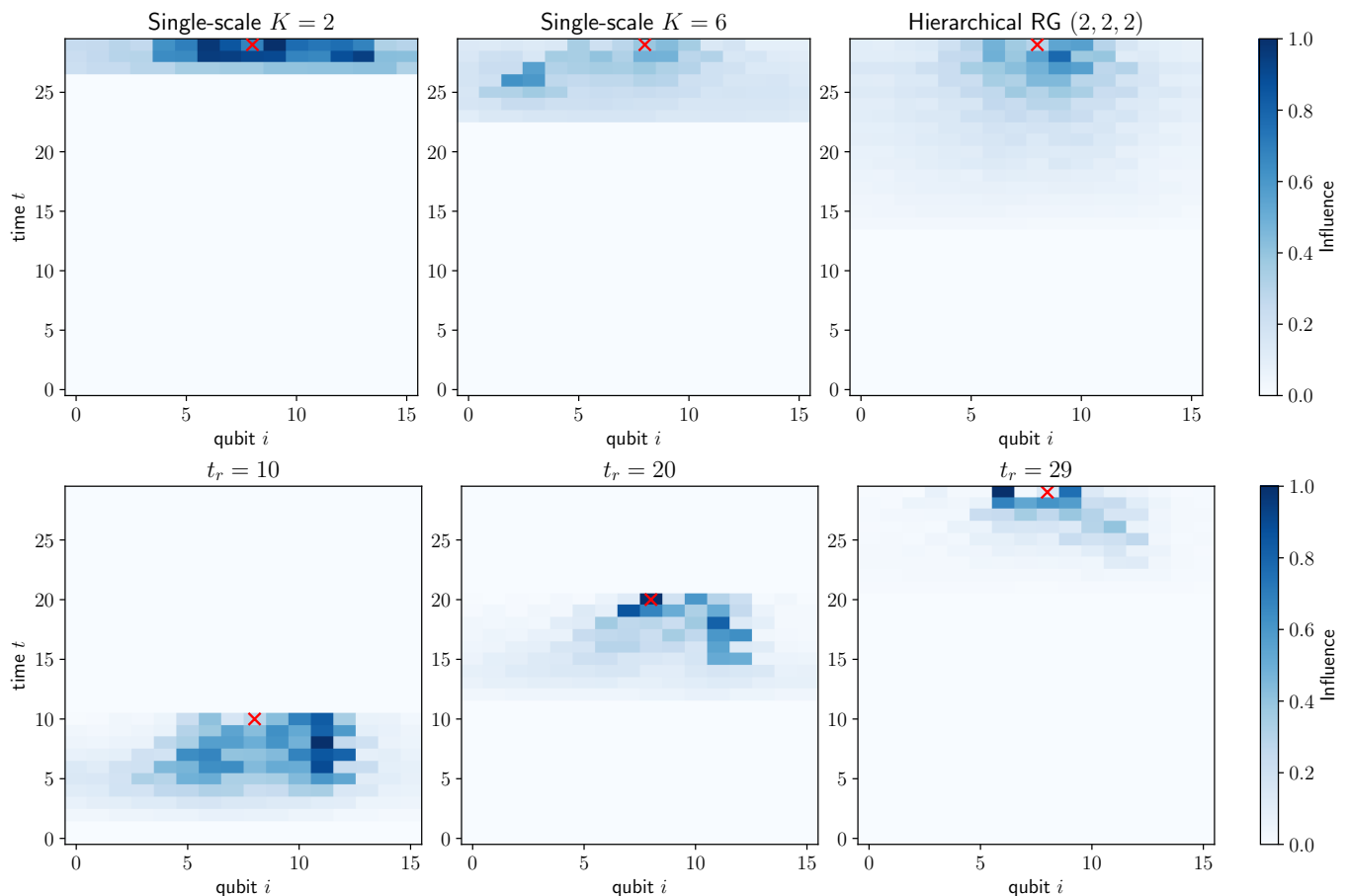


FIG. 7. Spacetime influence maps illustrating which measurement events (i, t) contribute most strongly to the neural-network prediction of the half-chain entropy. **(Top)** Influence maps for three representative architectures at $t_r = 30$: a shallow single-scale model ($K = 2$), a deeper single-scale model ($K = 6$), and a hierarchical RG(2, 2, 2) model. The red cross marks the readout location near the entanglement cut. **(Bottom)** Time-resolved influence maps obtained by evaluating the sensitivity of the prediction at different readout times $t_r = 10, 20, 29$ using single-scale model ($K = 6$). The dominant influence region shifts upward in time and expands as the readout time increases, indicating that the model integrates information from a growing spacetime region of the measurement record.

- [16] J. Gilmer, S. S. Schoenholz, P. F. Riley, O. Vinyals, and G. E. Dahl, Neural message passing for quantum chemistry, in *Proceedings of the 34th International Conference on Machine Learning*, ICML 2017 (PMLR, Sydney, Australia, 2017) pp. 1263–1272.
- [17] W. L. Hamilton, R. Ying, and J. Leskovec, *Inductive representation learning on large graphs* (2018), [arXiv:1706.02216 \[cs.SI\]](https://arxiv.org/abs/1706.02216).
- [18] T. N. Kipf and M. Welling, *Semi-supervised classification with graph convolutional networks* (2017), [arXiv:1609.02907 \[cs.LG\]](https://arxiv.org/abs/1609.02907).
- [19] E. H. Lieb and D. W. Robinson, The finite group velocity of quantum spin systems, *Communications in Mathematical Physics* **28**, 251–257 (1972).
- [20] B. Nachtergaele and R. Sims, *Lieb-robinson bounds in quantum many-body physics* (2010), [arXiv:1004.2086 \[math-ph\]](https://arxiv.org/abs/1004.2086).
- [21] Y. Bao, M. Block, and E. Altman, Finite-time teleportation phase transition in random quantum circuits, *Phys. Rev. Lett.* **132**, 030401 (2024).
- [22] Z. Cheng, R. Wen, S. Gopalakrishnan, R. Vasseur, and A. C. Potter, Universal structure of measurement-induced information in many-body ground states, *Phys. Rev. B* **109**, 195128 (2024).
- [23] M. N. Ivaki, T. Ojanen, and A. G. Moghaddam, Noise resilience in adaptive and symmetric monitored quantum circuits, *npj Quantum Information* **11**, [10.1038/s41534-025-01057-2](https://doi.org/10.1038/s41534-025-01057-2) (2025).